nature nanotechnology

LETTERS

PUBLISHED ONLINE: 13 OCTOBER 2013 | DOI: 10.1038/NNANO.2013.197

Electronic and plasmonic phenomena at graphene grain boundaries

Z. Fei[1], A. S. Rodin[2], W. Gannett[3,4], S. Dai[1], W. Regan[3,4], M. Wagner[1], M. K. Liu[1], A. S. McLeod[1], G. Dominguez[5,6], M. Thiemens[5], Antonio H. Castro Neto[2,7], F. Keilmann[8], A. Zettl[3,4], R. Hillenbrand[9,10], M. M. Fogler[1] and D. N. Basov[1]*

Graphene[1], a two-dimensional honeycomb lattice of carbon atoms of great interest in (opto)electronics[2,3] and plasmonics[4–11], can be obtained by means of diverse fabrication techniques, among which chemical vapour deposition (CVD) is one of the most promising for technological applications[12]. The electronic and mechanical properties of CVD-grown graphene depend in large part on the characteristics of the grain boundaries[13–19]. However, the physical properties of these grain boundaries remain challenging to characterize directly and conveniently[15–23]. Here we show that it is possible to visualize and investigate the grain boundaries in CVD-grown graphene using an infrared nano-imaging technique. We harness surface plasmons that are reflected and scattered by the graphene grain boundaries, thus causing plasmon interference. By recording and analysing the interference patterns, we can map grain boundaries for a large-area CVD graphene film and probe the electronic properties of individual grain boundaries. Quantitative analysis reveals that grain boundaries form electronic barriers that obstruct both electrical transport and plasmon propagation. The effective width of these barriers (~10–20 nm) depends on the electronic screening and is on the order of the Fermi wavelength of graphene. These results uncover a microscopic mechanism that is responsible for the low electron mobility observed in CVD-grown graphene, and suggest the possibility of using electronic barriers to realize tunable plasmon reflectors and phase retarders in future graphene-based plasmonic circuits.

Our imaging technique, which we refer to as 'scanning plasmon interferometry', is implemented in a setting of an antenna-based infrared nanoscope[6–8]. A schematic diagram of the scanning plasmon interferometry technique is shown in Fig. 1a. Infrared light focused on a metallized tip of an atomic force microscope (AFM) generates a strong localized field around the sharp tip apex, analogous to a 'lightning-rod' effect[24]. This concentrated electric field launches circular surface plasmons around the tip (pink circles in Fig. 1a). The process is controlled by two experimental parameters: the wavelength of light, λ_{IR}, and the curvature radius of the tip, R. To efficiently launch surface plasmons onto our highly doped graphene films, we chose infrared light with λ_{IR} close to 10 μm and AFM tips with $R \approx 25$ nm (see Methods). The experimental observable of the scanning plasmon interferometry is the scattering amplitude s, which is collected simultaneously with AFM topography.

Before analysing the grain boundaries, we first discuss a crack-type line defect with a geometric width of ~10 nm that is visible in the AFM topography (blue arrows in Fig. 1b). The corresponding scanning plasmon interferometry image is presented in Fig. 1c, where we plot the scattering amplitude s at $\lambda_{IR} = 11.3$ μm. The scattering signal shows bright twin fringes running along this line defect. In the same field of view, we also observe a region of double-layer graphene (blue dashed loop) and a microscopic line structure (green shaded region in Fig. 1b). All these features are commonly found in CVD graphene[12] (Supplementary Fig. S1a). The bright circular fringes are observed near the edge of the double-layer region (Fig. 1c). By tuning λ_{IR} from 11.3 μm (Fig. 1c) to 10.5 μm (Fig. 1d), the fringe widths of both types of fringes show evident λ_{IR} dependence, which is consistent with the plasmonic origin of these patterns[7,8]. Note that the scattering amplitude in all our scanning plasmon interferometry images is normalized to that of a sample region where no fringes exist (for example, the green square in Fig. 1c).

In previous studies[7,8], plasmon fringes with a width equal to half the plasmon wavelength, $\lambda_p/2$, were observed close to the edges of graphene microcrystals. To validate the plasmonic origin of the fringes found here, we plot in Fig. 1f the width of the twin fringes (circles) as a function of λ_{IR}. In the same plot we also present theoretical results (see Methods for details). The agreement between the experimental data and the calculated curve confirms that the bright fringes at the line defects are of plasmonic origin, in close analogy with the oscillations of the scattering amplitude at the edges of graphene. In either case, the near-field signal is formed by a standing wave with periodicity $\lambda_p/2$ produced by the interference between the tip-launched and reflected plasmons[7,8].

We observe twin fringes not only close to the cracks but also near other types of line defects that we identified as wrinkles and grain overlaps based on the AFM topography (Supplementary Fig. S2). However, the most prevailing line defects are grain boundaries (illustrated schematically in Fig. 1a with a red line). As a rule, grain boundaries are of atomic length scale, and are therefore invisible in typical AFM scans (Fig. 2a). Yet grain boundaries were vividly visualized by scanning plasmon interferometry, producing characteristic twin fringes (Fig. 2b,d). We examined the λ_{IR} dependence of the fringe width and found that it is in agreement with the theoretical calculation (red circles in Fig. 1f). This latter finding

[1]Department of Physics, University of California, San Diego, La Jolla, California 92093, USA, [2]Department of Physics, Boston University, Boston, Massachusetts 02215, USA, [3]Department of Physics and Astronomy, University of California, Berkeley, California 94720, USA, [4]Materials Sciences Division, Lawrence Berkeley National Lab, Berkeley, California 94720, USA, [5]Department of Chemistry and Biochemistry, University of California, San Diego, La Jolla, California 92093, USA, [6]Department of Physics, California State University, San Marcos, California 92096, USA, [7]Graphene Research Centre and Department of Physics, National University of Singapore, 117542, Singapore, [8]Ludwig-Maximilians-Universität and Center for Nanoscience, 80539 München, Germany, [9]CiC nanoGUNE Consolider, 20018 Donostia-San Sebastián, Spain, [10]IKERBASQUE, Basque Foundation for Science, 48011 Bilbao, Spain.
*e-mail: dbasov@physics.ucsd.edu

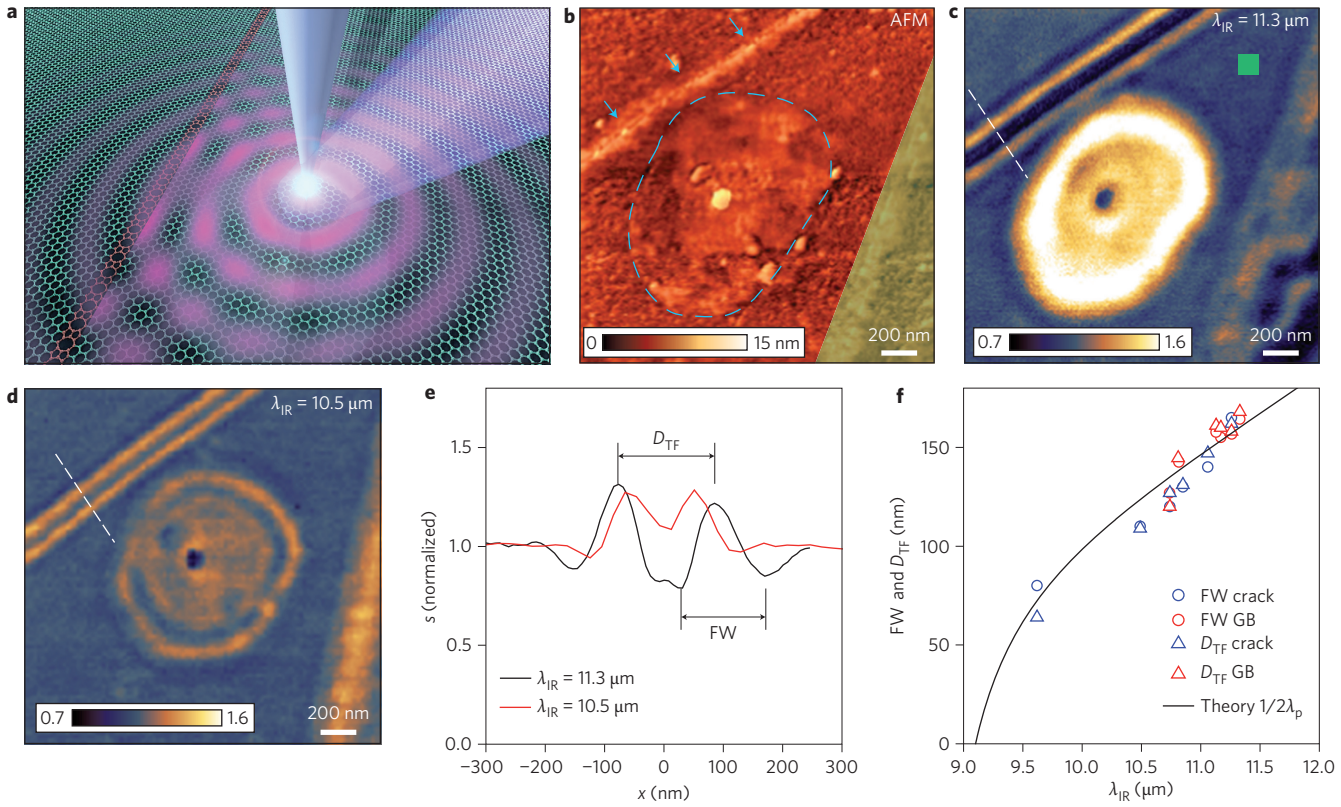

Figure 1 | Probing CVD graphene with scanning plasmon interferometry. a, Illustration of the scanning plasmon interferometry principle. The AFM tip (silver cone) illuminated with infrared light (purple cone) launches surface plasmon waves (pink circles) into graphene. These waves are partially reflected by the line defect (red line), causing interference between the launched and back-reflected plasmonic waves. **b**, AFM topography of CVD graphene revealing a crack-type line defect (blue arrows), a double-layer graphene region (blue dashed loop) and a microscopic line structure (green shaded region). **c**,**d**, Scanning plasmon interferometery images taken simultaneously with the AFM topography in **b** at infrared wavelengths of $\lambda_{IR} = 11.3$ μm (**c**) and 10.5 μm (**d**). **e**, Line profiles taken along the white dashed lines in **c** and **d**. Also illustrated, for the 11.3 μm case, is a protocol to extract the fringe width (FW) and the separation between the twin fringes D_{TF}. **f**, Evolution of FW (circles) and D_{TF} (triangles) with λ_{IR} for the crack in Fig. 1b (blue) and the grain boundary (GB) in Fig. 2 (red). The black solid line is a theoretical result for the magnitude of $1/2\lambda_p$ assuming a Fermi energy of $E_F \approx 0.37$ eV (see Methods). Note that λ_p decreases rapidly for $\lambda_{IR} < 10$ μm, a consequence of plasmon coupling to the surface optical phonon of SiO_2. The data range for grain boundaries is narrower than that of the crack due to the fact that the grain boundary is a less efficient plasmon reflector than the crack. Scanning plasmon interferometry images **c** and **d** show the normalized amplitude *s* of the nano-optic signal as described in the text.

attests to the plasmonic origin of the scanning plasmon interferometry signal at grain boundaries.

So far, we have mainly discussed the fringe width, which is a direct measure of λ_p. Yet another important parameter is the separation between twin fringes D_{TF} (Fig. 1e). For grain boundaries, D_{TF} can be written as $D_{TF} \approx (-\delta/2\pi)\lambda_p$, where δ is the plasmon phase shift on reflection off a grain boundary set to vary within $[-2\pi, 0]$ (Supplementary equation (S19)). Therefore, for a non-zero constant δ, the magnitude of D_{TF} is proportional to λ_p, which is indeed confirmed by our experiment (Fig. 1f). Our data indicate that D_{TF} roughly equals $1/2\lambda_p$ for all grain boundaries, so δ is close to $-\pi$. Note that the parameter δ is not solely determined by the response of our graphene samples. The AFM tip also plays an important role here. As detailed in Supplementary Section S4, it is convenient to write δ as $\delta = \delta_{sp} + \delta_t$, where δ_{sp} is the plasmon phase shift without tip coupling to graphene, and δ_t is a tip-dependent parameter that is around $-(0.5 \pm 0.1)\pi$ based on our numerical modelling (Supplementary equation (S19)).

The above analysis for D_{TF} also holds true for other types of line defects with geometric features much smaller than λ_p, such as the crack shown in Fig. 1b. Nevertheless, for line defects such as wrinkles and grain overlaps (Supplementary Fig. S2), the twin fringes are strongly affected by their geometric form. As detailed in Supplementary Section S2, these two types of line defects generate twin fringes with considerable variations of D_{TF} governed by the details of a particular defect. A unique feature of grain boundaries and grain overlaps is that they together form a network of closed regions (grains) spanning over the entire graphene film (Fig. 2e, Supplementary Fig. S3). In contrast, cracks and wrinkles are sporadic and discontinuous. From Fig. 2e, we were able to measure the average grain size (3–5 μm) of our film, in agreement with reports for graphene prepared under identical conditions[21].

To gain a quantitative understanding of the twin fringes in our scanning plasmon interferometry images, we performed numerical modelling, taking into account all the experimental details. In our modelling, we assumed that grain boundaries locally modify the plasmon wavelength λ_p and damping rate γ_p. Here, γ_p is defined by the ratio between the imaginary and real parts of the plasmon wavevector $q_p \equiv (2\pi/\lambda_p)(1 + i\gamma_p)$. We found that the profiles of $\lambda_p(x)$ and $\gamma_p(x)$ displayed in Fig. 2f produce an accurate fit for the experimental data taken at multiple λ_{IR} in the range of 10.7–11.3 μm (Fig. 2c, Supplementary Fig. S7). Details of the modelling are given in Supplementary Section S5. The fact that the single set of parameters fits the totality of fringe profiles indicates that the choice of these parameters is quite robust. For example, an assumption of a dip in $\lambda_p(x)$ as opposed to a peak at the grain boundary would almost double D_{TF} (see Supplementary Fig. S5a and the following paragraphs). We note that strong scattering quantified

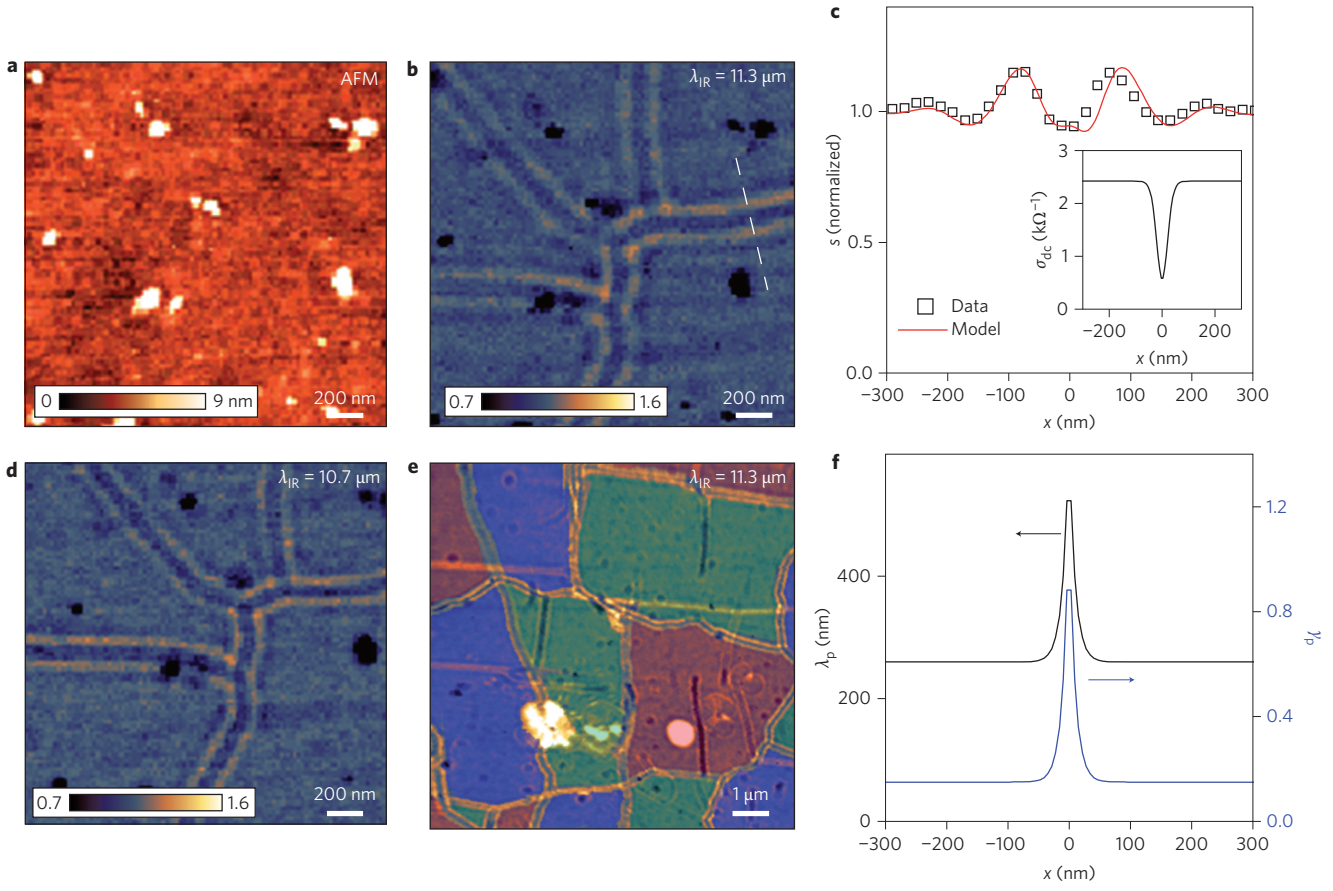

Figure 2 | Grain boundaries observed in CVD graphene films. a, Topography image of graphene containing grain boundaries. **b**, Scanning plasmon interferometry image taken at the same time as **a** at $\lambda_{IR} = 11.3$ μm, revealing grain boundaries. **c**, Experimental (black squares) and modelled (red curves) twin fringe profiles. The experimental profile is taken along the dashed line in **b**. Inset: profile of d.c. conductivity inferred from modelling. **d**, Scanning plasmon interferometry image of the sample area in **b** taken at $\lambda_{IR} = 10.7$ μm. **e**, A larger-area scan of a typical sample revealing multiple grains (displayed with different false colours) defined by the twin fringes due to grain boundaries and grain overlaps. Details of line-defect arrangements in this map are given in Supplementary Fig. S3. **f**, Profiles of plasmon wavelength λ_p and damping rate γ_p used for modelling the fringe profiles of the grain boundary shown in **c** and Supplementary Fig. S7.

with γ_p in concert with the enhancement of λ_p at the grain boundary is needed to reproduce the line shape of the twin fringes.

We now discuss some of the implications of our modelling. According to the plasmon dispersion equation (see Methods), λ_p is roughly proportional to E_F. In turn, E_F scales as a square root of the carrier density n. Thus, our results imply that our graphene film tends to be heavily doped with $n \approx 4 \times 10^{13}$ cm^{-2} at the grain boundaries, corresponding to 0.021 holes per unit cell. This is expected, because grain boundaries are lattice defects that favour molecule adsorptions at ambient conditions[25,26]. The role of defects in enhancing doping due to molecule adsorption has been extensively studied previously[27,28]. In contrast, under ultra-high-vacuum conditions, where molecule adsorption is significantly reduced, graphene films are close to the charge neutrality point and grain boundaries perturb the electronic properties of graphene in a totally different way, as confirmed by scanning tunnel microscopy studies[18]. The plasmon damping rate depends on the carrier scattering rate of graphene, τ^{-1}, where $\gamma_p \approx 0.05 + (\omega\tau)^{-1}$ (Supplementary equation (S21)). Therefore, the lineform of $\gamma(x)$ inferred from modelling implies that charge carriers experience enhanced scattering close to the grain boundaries. We speculate that this effect may be caused by Coulomb scattering due to the charges at the grain boundaries. Furthermore, modelling indicates that grain boundaries perturb the electronic properties over a length scale of the order of 20 nm. A wider effective width compared to the geometric width is in fact an outcome of electron screening of the charged grain boundaries[29]. Indeed, the charge screening length is estimated to be on the order of the Fermi wavelength, ~10 nm in our doping range, which is consistent with our experimental findings.

Based on the $\lambda_p(x)$ and $\gamma_p(x)$ profiles in Fig. 2f, we can calculate the $E_F(x)$ and $\tau^{-1}(x)$ profiles across the grain boundaries. These latter parameters allow us to infer the d.c. conductivity σ_{dc} of graphene (inset of Fig. 2c) with a standard formula[11]: $\sigma_{dc} \approx (2e^2/h)(E_F/\hbar\,\tau^{-1})$. This equation is obtained by assuming weak frequency dependence of τ^{-1} that is valid when Coulomb scattering dominates[11]. Although the increase of E_F near the grain boundaries would normally boost σ_{dc}, this expected trend is overwhelmed by the increase in τ^{-1}. The net effect for grain boundaries is to significantly reduce the local σ_{dc} of graphene.

Finally, we wish to point out that the plasmon reflection off grain boundaries can be described by a reflection coefficient r_{sp}. By analytically solving the problem of surface plasmon scattering by grain boundaries, we were able to obtain the formula $r_{sp} \approx iW_{eff}\Delta q_p$ (Supplementary equation (S14)), where Δq_p is the relative change of plasmon wavevector due to the grain boundaries and W_{eff} is the effective width. Based on r_{sp}, we were able to estimate both the plasmon reflection probability $|r_{sp}|^2$ and the phase shift $\delta_{sp} = \arg(r_{sp})$. The former is closely related to the fringe intensity, and the latter determines D_{TF}, as discussed above. Calculations

based on the λ_p and γ_p profiles of the grain boundary (Fig. 2f) yield $|r_{sp}|^2 \approx 8\%$ and $\delta_{sp} \approx -0.6\pi$. The 8% reflectivity is remarkably high. Such a strong reflection is due to the extended effective width of the electronic perturbation induced by the grain boundaries (Fig. 2f). A phase shift of $\delta_{sp} \approx -0.6\pi$ is an outcome of higher doping at the grain boundary. If one switches the grain boundary to a lower doping, δ_{sp} will undergo a 'π' phase shift and become -1.6π, resulting in a dramatic increase of D_{TF} away from the experimental value (Supplementary Fig. S5a). The above analysis indicates that $|r_{sp}|^2$ and δ_{sp} are sensitive to the doping of the plasmon reflector. Therefore, both parameters governing plasmon propagation can be conveniently tunable by common electronic means, such as electrostatic gating.

Our work provides unambiguous experimental evidence of novel plasmonic effects originating from plasmon reflection at grain boundaries in CVD graphene. The scanning plasmon interferometry technique, aided with modelling, is a comprehensive method capable of mapping and probing the electronic properties of grain boundaries. This method can be applied to nanocharacterization of plasmonic materials beyond graphene, where grain boundaries also play important roles in the plasmonic effects[30]. Moreover, our work provides guidelines to designing tunable electronic barriers that would realize reconfigurable plasmon reflectors[4] and phase retarders—a milestone towards graphene-based plasmonic circuits.

Methods

Samples. Our graphene films were grown on copper foils using a two-step low-pressure CVD method[12], then transferred to silicon wafers with a 300 nm SiO_2 layer on top. All experiments were performed under ambient conditions and in an atmospheric environment. The graphene films were unintentionally hole-doped with a carrier density of $\sim 1.0 \times 10^{13}$ cm^{-2} corresponding to a Fermi energy E_F of 0.37 eV. Such high doping is due to the SiO_2 substrate, as well as molecule adsorption in the air atmosphere[26,27]. The doping level was inferred from our Raman and near-field gating experiments (Supplementary Section S1).

Experimental apparatus. The scanning plasmon interferometry experiments introduced in the main text were performed at UCSD using a scattering-type scanning near-field optical microscope (s-SNOM)[24]. Our s-SNOM is a commercial system (neaspec.com) equipped with mid-infrared quantum cascade lasers (daylightsolutions.com) and CO_2 lasers (accesslaser.com) covering a wavelength range of 9.5–11.3 μm. The s-SNOM, equipped with a pseudo-heterodyne interferometric detection module, is based on an atomic force microscope (AFM) operating in the tapping mode with a tapping frequency around 270 kHz. The output signal of s-SNOM utilized in this work is the scattering amplitude s demodulated at nth harmonics of the tapping frequency ($n = 2$ in the current work).

To efficiently couple infrared light to the graphene plasmons, an AFM tip with a radius of $R \approx 25$ nm was chosen as our near-field probe. This scheme allowed us to overcome the notorious 'momentum mismatch' between plasmons and photons. As detailed in ref. 13, the momenta-coupling function has a bell-shaped momenta distribution that peaks at $q \approx 1/R$. For a typical CVD graphene film on an SiO_2 substrate, the momentum of infrared plasmons under ambient conditions lies between 3×10^5 and 6×10^5 cm^{-1}. Therefore, the optimum tip radius for exciting the surface plasmons of graphene in our frequency range is ~20–30 nm.

Evaluating the plasmon dispersion in graphene. The plasmon dispersion equation of graphene[7,11] at the interface between the air and the SiO_2 substrate with dielectric function $\varepsilon_{sub}(\omega)$ is given as $q_p = (i2\omega\varepsilon_0\kappa(\omega)/\sigma(\omega))$, where $\omega = 2\pi c/\lambda_{IR}$ is the infrared excitation frequency, $\kappa(\omega) = [1 + \varepsilon_{sub}(\omega)]/2$ is the effective dielectric function of the environment for graphene, and $\sigma(\omega)$ is the optical conductivity of graphene. The plasmon wavelength λ_p of graphene can be obtained with $\lambda_p = 2\pi/\mathrm{Re}(q_p)$. The optical conductivity we used to calculate the plasmon wavelength (×1/2) in Fig. 1f was obtained from the random phase approximation method[6,7]. We find excellent agreement between the experimental data and calculations of $1/2\lambda_p$ assuming a Fermi energy of $E_F \approx 0.37$ eV, which is in accord with our Raman measurements.

Alternatively, one can use a Drude formula that is valid at a limit of long wavelength and low frequency, $\sigma(\omega) = i(e^2/\pi\hbar^2)(E_F/\omega + i\tau^{-1})$, where e is the elementary charge, $\hbar$ is the reduced Planck constant, and τ^{-1} is the charge scattering rate in graphene. In this case, the plasmon wavelength λ_p adopts the analytic form $\lambda_p \approx (e^2 E_F \lambda_{IR}^2/h^2 c^2 \varepsilon_0 \mathrm{Re}\kappa)$.

Received 16 April 2013; accepted 6 September 2013; published online 13 October 2013

References

1. Geim, A. K. & Novoselov, K. S. The rise of graphene. *Nature Mater.* **6,** 183–191 (2007).
2. Castro Neto, A. H., Guinea, F., Peres, N. M. R., Novoselov, K. S. & Geim, A. K. The electronic properties of graphene. *Rev. Mod. Phys.* **81,** 109–162 (2009).
3. Bonaccorso, F., Sun, Z., Hasan, T. & Ferrari, A. C. Graphene photonics and optoelectronics. *Nature Photon.* **4,** 611–622 (2010).
4. Vakil, A. & Engheta, N. Transformation optics using graphene. *Science* **332,** 1291–1294 (2011).
5. Ju, L. *et al.* Graphene plasmonics for tunable terahertz metamaterials. *Nature Nanotech.* **6,** 630–634 (2011).
6. Fei, Z. *et al.* Infrared nanoscopy of Dirac plasmons at the graphene–SiO_2 interface. *Nano Lett.* **11,** 4701–4705 (2011).
7. Fei, Z. *et al.* Gate-tuning of graphene plasmons revealed by infrared nano-imaging. *Nature* **487,** 82–85 (2012).
8. Chen, J. *et al.* Optical nano-imaging of gate-tunable graphene plasmons. *Nature* **487,** 77–81 (2012).
9. Yan, H. *et al.* Tunable infrared plasmonic devices using graphene/insulator stacks. *Nature Nanotech.* **7,** 330–334 (2012).
10. Grigorenko, A. N., Polini, M. & Novoselov, K. S. Graphene plasmonics. *Nature Photon.* **6,** 749–758 (2012).
11. Jablan, M., Buljan, H. & Slojačić, M. Plasmonics in graphene at infrared frequencies. *Phys. Rev. B* **80,** 245435 (2009).
12. Li, X. *et al.* Large-area synthesis of high-quality and uniform graphene films on copper foils. *Science* **324,** 1312–1314 (2009).
13. Grantab, R., Shenoy, V. B. & Ruoff, R. S. Anomalous strength characteristics of tilt grain boundaries in graphene. *Science* **330,** 946–948 (2010).
14. Wei, Y. *et al.* The nature of strength enhancement and weakening by pentagon–heptagon defects in graphene. *Nature Mater.* **11,** 759–763 (2012).
15. Yu, Q. *et al.* Control and characterization of individual grains and grain boundaries in graphene grown by chemical vapour deposition. *Nature Mater.* **10,** 443–449 (2011).
16. Song, H. S. *et al.* Origin of the relatively low transport mobility of graphene grown through chemical vapor deposition. *Sci. Rep.* **2,** 337 (2012).
17. Tsen, A. W. *et al.* Tailoring electrical transport across grain boundaries in polycrystalline graphene. *Science* **336,** 1143–1146 (2012).
18. Koepke, J. C. *et al.* Atomic-scale evidence for potential barriers and strong carrier scattering at graphene grain boundaries: a scanning tunneling microscopy study. *ACS Nano.* **7,** 75–86 (2013).
19. Tapasztó, L. *et al.* Mapping the electronic properties of individual graphene grain boundaries. *Appl. Phys. Lett.* **100,** 053114 (2012).
20. Huang, P. Y. *et al.* Grains and grain boundaries in single-layer graphene atomic patchwork quilts. *Nature* **469,** 389–392 (2011).
21. Kim, K. *et al.* Grain boundary mapping in polycrystalline graphene. *ACS Nano* **5,** 2142–2146 (2011).
22. Duong, D. L. *et al.* Probing graphene grain boundaries with optical microscopy. *Nature* **490,** 235–239 (2012).
23. Kim, D. W., Kim, Y. H., Jeong, H. S. & Jung, H. T. Direct visualization of large-area graphene domains and boundaries by optical birefringency. *Nature Nanotech.* **7,** 29–34 (2011).
24. Atkin, J. M., Berweger, S., Jones, A. C. & Raschke, M. B. Nano-optical imaging and spectroscopy of order, phases, and domains in complex solids. *Adv. Phys.* **61,** 745–842 (2012).
25. An, J. *et al.* Domain (grain) boundaries and evidence of 'twinlike' structures in chemically vapor deposited grown graphene. *ACS Nano* **5,** 2433–2439 (2011).
26. Ryu, S. *et al.* Atmospheric oxygen binding and hole doping in deformed graphene on a SiO_2 substrate. *Nano Lett.* **10,** 4944–4951 (2010).
27. Das, A., Chakraborty, B. & Sood, A. K. Raman spectroscopy of graphene on different substrates and influence of defects. *Bull. Mater. Sci.* **31,** 579–584 (2008).
28. Kim, D. C. *et al.* The structural and electrical evolution of graphene by oxygen plasma-induced disorder. *Nanotechnology* **20,** 375703 (2009).
29. Radchenko, T. M., Shylau, A. A. & Zozoulenko, I. V. Effect of charged line defects on conductivity in graphene: numerical Kubo and analytical Boltzmann approaches. *Phys. Rev. B* **87,** 195448 (2013).
30. Lu, Y-J. *et al.* Plasmonic nanolaser using epitaxially grown silver film. *Science* **337,** 450–453 (2012).

Acknowledgements

The authors acknowledge support from the Office of Naval Research. The development of scanning plasmon interferometry is supported by the US Department of Energy Office of Basic Energy Sciences. G.D. and M.T. were supported by the National Aeronautics and Space Administration (grant no. NNX11AF24G). M.F. is supported by the University of California Office of the President and the National Science Foundation (PHY11-25915).

A.H.C.N. acknowledges a Singapore National Research Foundation Competitive Research Programme grant (R-144-000-295-281). M.W. thanks the Alexander von Humboldt Foundation for financial support. R.H. acknowledges a European Research Council starting grant (no. 258461). A.S.M. is supported by a US Department of Energy Office of Science Graduate Fellowship.

Author contributions

All authors were involved in designing the research, performing the research and writing the paper.

Additional information

Supplementary information is available in the online version of the paper. Reprints and permissions information is available online at www.nature.com/reprints. Correspondence and requests for materials should be addressed to D.N.B.

Competing financial interests

F.K. and R.H. are cofounders of Neaspec, producer of the s-SNOM apparatus used in this study.